TEM analysis and molecular dynamics simulation of graphene coated Al-Cu micro joints

Omkar Mypati , Polkampally Pavan Kumar , Surjya Kanta Pal , Prakash Srirangam

PII: S2667-0569(22)00079-7
DOI: https://doi.org/10.1016/j.cartre.2022.100223
Reference: CARTRE 100223

To appear in: *Carbon Trends*

Received date: 8 February 2022
Revised date: 15 October 2022
Accepted date: 15 October 2022

Please cite this article as: Omkar Mypati , Polkampally Pavan Kumar , Surjya Kanta Pal , Prakash Srirangam , TEM analysis and molecular dynamics simulation of graphene coated Al-Cu micro joints, *Carbon Trends* (2022), doi: https://doi.org/10.1016/j.cartre.2022.100223

TEM analysis and molecular dynamics simulation of graphene coated Al-Cu micro joints

Omkar Mypati[a], Polkampally Pavan Kumar[b], Surjya Kanta Pal[a*], Prakash Srirangam[c]

[a]Department of Mechanical Engineering, Indian Institute of Technology Kharagpur, 721302, India, Email: omkar.mypati@iitkgp.ac.in (Omkar Mypati), skpal@mech.iitkgp.ac.in (Surjya Kanta Pal)

[b]Department of Metallurgical and Materials Engineering, Indian Institute of Technology Kharagpur, 721302, India, Email: p.pavanlgl@gmail.com (Polkampally Pavan Kumar)

[c]Warwick Manufacturing Group, University of Warwick, CV4 7AL, UK, Email: P.Srirangam@warwick.ac.uk (Prakash Srirangam)

***Corresponding author:** Surjya Kanta Pal

Abstract

This study compares friction-stir spot welds (FSSW) of pure Al to Cu, with and without graphene interlayer (GL), for tensile load and electrical conductivity (σ). The weld interface of Al-Cu fabricated without a GL is found with brittle intermetallic compounds (IMC) like Al_2Cu. The presence of brittle IMCs significantly affects the tensile load and σ. In contrast, the sample with GL suppresses the brittle IMCs and enhances the formation of Al_4C_3 IMC. The presence of Al_4C_3 strengthens the weld joint by 26.94 % concerning the without GL samples. Further, it was observed that thinner and high-density twins are formed in the samples with GL. The formation of thinner deformation twins is also possible for increased tensile load and σ. The thicker twins in the samples without GL inhibit the electron flow and increase electrical resistivity. The molecular dynamics (MD) simulation was performed to study the in-situ formation of deformed twins. In addition, the MD simulation provides insight into the influence of graphene during the formation of IMCs based on diffusion coefficients of individual atoms. The σ of the Al-Cu joint can be estimated using a cluster Nernst-Einstein equation, which is dependent on the diffusion coefficient obtained from MD simulation.

Keywords: Friction stir spot welding; Graphene; Molecular dynamic simulation; Intermetallic compounds; Twin boundaries; Electrical conductivity

1. Introduction

As energy exhaustion and global climate change increase, the automotive industry is looking for alternative energy sources. Consequently, electric vehicles (EVs) have become a prominent automobile industry solution [1]. Lithium-ion (Li-ion) batteries are frequently used in EVs due to high energy, power density, and less self-discharge characteristics [2,3]. Typically, a Li-ion battery pack consists of several cells connected by welding the current collectors and busbars with a current collector to form a series and parallel cell combinations, respectively [4–6]. However, the current collectors are designed to be dissimilar combinations due to the difference in oxidation potentials at the cathode and anode. A Li-ion battery cathode and anode potential range from ~3 to 4.5 V vs. Li/Li^+ and ~0.01 to 2.5 V vs. Li/Li^+, respectively [7,8]. Aluminum (Al) with a higher oxidation potential is used as a cathode current collector, while copper (Cu) with a lower potential is used as an anode current collector [9]. Moreover, Al and Cu are highly conductive materials of electricity. Based on these observations, many researchers consider Al and Cu materials as current collectors. A challenge in the battery pack fabrication is the joining of current collectors due to their dissimilar material combinations [4,6]. A major problem associated with joining dissimilar materials is the difference in melting points. Other issues include crack formation, unbonded interfaces, brittle intermetallic compounds (IMC), metallurgical defects, etc. [10–12]. These defects lead to an energy loss in batteries and even result in battery failure. Because of their different melting points and chemical properties, dissimilar metals exhibit poor fusion weldability. The Al-Cu joints manufactured using fusion welding had inadequate bonding and poor electrical properties due to the oxide layers formed on the Al substrate [13]. Although Al and Cu welding pose slightly different challenges for all welding processes, the main problem is the formation of brittle IMCs during welding [14]. High heat input during fusion welding results in the formation of more Al_2Cu IMC. In order to reduce the formation of brittle IMCs, research towards solid-state joining is increased.

The authors suggest that solid-state welding is superior to other fusion welding techniques because of reduced thermal defects, crack formation and reduces brittle IMC formation during Al and Cu joining [15–17]. A few solid-state welding methods include ultrasonic welding, diffusion

welding, and friction stir spot welding (FSSW). In addition to solid-state welding, other welding techniques like resistance spot welding and laser beam welding are prominently used in Li-ion battery manufacturing [18]. Due to significant research and development on dissimilar materials joining, FSSW has gained significant importance in industries. By optimizing FSSW process parameters, it is possible to obtain high-quality Al-Cu dissimilar joints with reduced IMC formation and increased mechanical and electrical properties. Shiraly et al. [19] stated the tensile failure load was found to be influenced by the stirring zone length. However, it did not examine the effect of metallurgical bonding and the IMC formation at Al-Cu interfaces [19]. Though the FSSW technique reduces the IMC formation compared to fusion joining methods, it is challenging to completely eliminate them as Al and copper have negative mixing of enthalpy, which results in the formation of IMCs in the joint. In addition, the IMCs are formed by mixing detached Cu particles embedded in the Al matrix [20]. The IMCs like Al_2Cu, AlCu, and Al_4Cu_9 are observed in the case of the FSSW of Al and Cu [4,21]. In response to the brittle IMCs presence in between the Al–Cu interface, FSSW has been developed for dissimilar material joining with introducing an interlayer in minimizing the formation of more brittle IMCs.

The interlayers like zinc (Zn) [22,23], and Titanium (Ti) [23], etc., are used to enhance the mechanical properties during Al-Cu FSSW conditions. The samples welded with Ti and Zn interlayers have obtained higher ultimate tensile strength (UTS) values and reduced the formation of brittle IMCs compared to the FSSW of Al-Cu samples. The decrease in the formation of IMCs in the nugget zone (NZ) is due to the Ti interlayer acting as a diffusion layer. In contrast, the Zn interlayer behaves as an alloying element [23]. The Zn has a high affinity with Cu and forms $CuZn_5$ and $Al_{4.2}Cu_{3.2}Zn_{0.7}$ (τ') IMCs [24]. Although Zn interlayers enhance mechanical strength, it has not been used as an interlayer to improve the electrical properties of a weld joint due to lower electrical conductivity. In this regard, the authors used graphene as an important alternative interlayer due to its higher strength, thermal conductivity, and σ as compared to other interlayer materials [25,26]. Montazerian et al. [27] introduced the graphene nanoparticles in the weld interface and observed an increase in the tensile load and a ~40 % decrease in electrical resistivity. During the welding process, submicron size fragmented graphene particles can impinge on grain boundaries and reduce grain size, which improves mechanical properties [27]. The graphene material is effective in barricading against the migration of dislocations to enhance the tensile load. Moreover, graphene improves the mixing

of materials at optimum temperature and reduces the formation of voids in the weld NZ. The mechanical and electrical properties are further explained based on twins formation. A simple analysis of energy can be used to examine twinning's origin. A face-centered cubic (FCC) metals with low stacking-fault energy exhibit significant deformation twin structures. In order to form a twin boundary, there needs to be a single plane of atoms between two non-mixing phases. During aging treatment, the precipitates inhibit the movement of twin boundaries and increase the strength of the matrix. The decrease in solute content, i.e., an increase in twin density in the welded sample during the process had a positive effect on the electrical properties [28]. To estimate the IMC formation and deformation twins in the sample required several post-processing techniques. Zhang et al. [29] used Molecular dynamic (MD) simulation to interpret the microscopic changes in the system during the application of process conditions.

The MD simulation reveals the evolution of microstructure, which interprets the mechanism of FSSW on a microscopic level. The MD simulation can be used to investigate microstructure variations, diffusion behavior, and IMC formation concerning the given welding conditions [30]. Chen et al., studied the MD simulation between Cu/Ag diffusion bonding and observed an amorphous interfacial region. The increase in diffusion pressure results in the formation of a thicker weld interface zone [31]. The metallurgical phenomenon at the Al-Cu joint interface in the MD simulation found that dislocation accumulation resulted in forming a transition layer with amorphous nanocrystalline phases [21]. The diffusivity of Cu into the Al is directly dependent on the rise in temperature [32]. There is no significant study done on the MD simulation of Al-Cu FSSW with graphene as an interlayer. However, the effect of graphene in the metal composite using MD is studied. Accordingly, Zhang et al., stated graphene boundaries with Cu nanocomposite exhibit the highest strength and strain hardening capacity compared to non-crystalline/Cu. By substituting graphene boundaries, conventional grain boundaries are refused to self-deformation and show the high strength resulting from intragranular dislocation mediated processes [29]. Generally, to obtain the σ of an Al-Cu joint, a 4-probe electrical conductivity post-analysis is needed to be performed [4]. Using the diffusion coefficients obtained from the MD simulation, the σ of an FSSW can be determined using a Nernst-Einstein (NE) equation. However, NE is restricted to measure a individual atoms/ion conductivity. In this regard, a cluster Nernst-Einstein equation is developed, where atoms/ions form clusters, and the σ is measured based on the diffusivity [33].

The present study investigates the mechanical properties, metallurgical characterization, and electrical properties of FSSWed dissimilar Al-Cu welds. In addition, the effect of GL at the weld interface is explicitly studied by electron back-scattered diffraction (EBSD) and transmission electron microscopy (TEM) analyses. The MD simulations are performed for the FSSW conditions to learn critical insights on the formation of IMCs, deformation twins, diffusion behavior of atoms, and σ of the welding joints. Further, the obtained σ from the MD simulations are studied using the bonding mechanism and further correlated with X-ray photoelectron spectroscopy (XPS).

2. Experimental and simulation procedure

The Al-Cu welding has been performed using a linear FSW machine (WS004, ETA Technologies Bangalore). The base materials of 500 μm thick pure Cu are placed over the 500 μm thick pure Al in a lap welding configuration, as shown in Fig. 1 (c). The oxide layer over the Al substrate is removed using manual polishing with a 220 grid size. In addition, three experiments are performed using the GL in between Al and Cu. The graphene used in the current study is commercially procured from United-Nanotech Pvt. Ltd., India, and is mixed with a polyvinyl alcohol (Sigma-Aldrich, Germany) in order to obtain an even coating over the Al substrate as shown in Fig. 1(b). In order to remove solvent traces from the coating, the coated sample is placed in a vacuum furnace for 1 h at 100 ºC. Then a coating of ~150 μm graphene layer is applied on Al substrate using a tape casting method as depicted in Fig. 1 (b). Table 1 lists the process parameters employed, in which the plunge depth and the dwell time are kept constant for all weld samples at 0.2 mm and 15 seconds, respectively. For each condition of the process parameters, three welds are performed and the results are correlated with the reproducibility of the welded samples.

Table 1. Process parameters with the sample nomenclature

Sample nomenclature	Without GL			With GL		
	S_{500}	S_{1500}	S_{2500}	S_{GL-500}	$S_{GL-1500}$	$S_{GL-2500}$
Rotational speed ω (rpm)	500	1500	2500	500	1500	2500

FSSW is performed using an H13 grade steel tool with an 8 mm shoulder diameter, 3 mm pin diameter, and 0.4 mm pin height as shown in Fig. 1 (c). The temperature variation due to the process parameters of the weld joints has been captured using a thermal imaging camera (E95, Flir). Fig. 1 (d), illustrate the thermal vision space created by the thermal imaging camera during the weld process. The spot welded samples are cut in a dimesion of 100 mm X 10 mm as showin in Fig. 1 (c). Further, the welded samples are subjected to tensile testing using (ZwickRoell, Kappa 100 SS-CF testing machine). The tensile load of base Al is found to be 1355.6 N. The cross-section of Al-Cu welded samples are cut with a dimesions of 8 mm X 1 mm and mounted using a hot mounting press (Struers, Citopress) to perform the metallurgical characterizations. The sample used for the characterization was obtained from the weld interface, as shown in Fig. 1 (e). Mounted samples are polished with 300 to 3000 grit size emery paper, and finally the samples are polished with diamond polish whose particles have a size of 1 μm. The IMC at the joint interface are studied using X-Ray diffraction (PANalytical B.V, 7602 EA) with Cu source and maintaining a voltage of 40 kV and current of 40 mA within a range from 20° to 120°. The electrical resistivity has been measured with a 4-probe electrical conductivity setup (Ecopia, 0.545T). In order to obtain an accurate electrical resistance value, the sample dimensions are fed into the 4-probe setup. By reciprocating the resistance values, the electrical conductivity of the welded samples is calculated. To analyze the welded samples microstructure, scanning electron microscopy (Zeiss, Merlin) was used for obtaining graphene layer structure as shown in Fig. 1 and also perform the EBSD analysis. In an EBSD analysis, a focused ion beam is used to measure the microstructure of the welded sample. To obtain a fine polish, weld samples are polished up to 80 μm in size and then subjected to low-energy Ar^+ ion beam milling up to 2-3 hours maintained at 6 KeV until a perforation is evident on the surface of the sample. After, the formation of IMCs has been analyzed using TEM (JEM 2100F, JEOL). XPS analyses (PHI5000VersaProbe III, ULVAC-PHI, Inc) was performed at 0.2 kV voltage and 100 mA current to study the chemical composition and evaluate the oxidation state of the elements present in the weld interface.

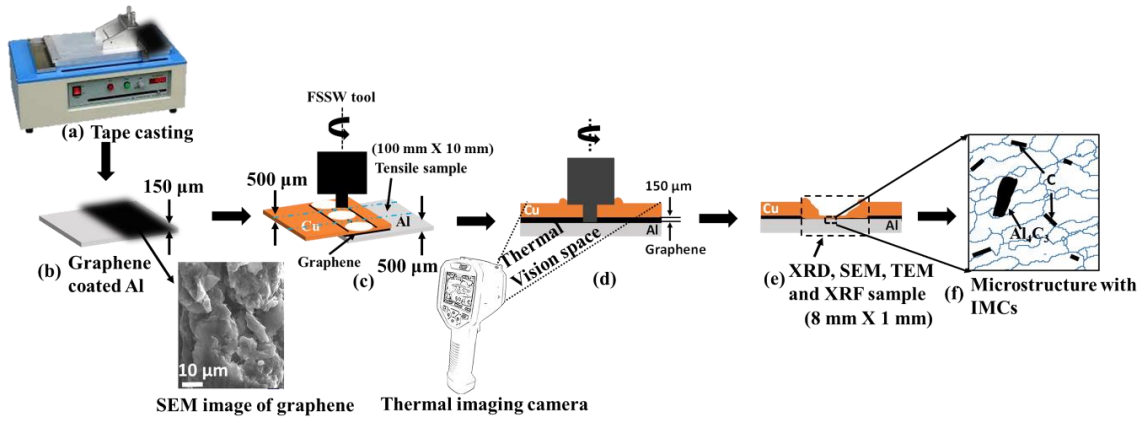

Fig 1. Schematic of an experimental and characterization procedure

MD simulations for the samples without and with GL is performed using large-scale atomic/molecular massively parallel simulator (LAMMPS) packages. The interatomic interaction of Al and Cu is defined using an embedded atom method potential (EAM) [21], the interaction between the carbon (C) atoms is defined using Airebo potentials [34], and interaction between Al-C-Cu is specified using a 12-6-Lennard-Jones (LJ) potential, as shown in Table 2 [35,36].

Table 2. 12-6-LJ potentials

Atoms interactions	Energy, ε (eV)	Distance (Å)
Al-Al	0.05	2.85
Cu-Cu	0.0168	2.2
Al-C	0.035	3.013
Cu-C	0.02578	3.08

The simulation box size for without and with GL is 51.6 Å × 108.46 Å × 108.46 Å and 27.94 Å × 18.68 Å × 51.18 Å, respectively. The simulation box size is chosen arbitrary to determine the group of atoms and to optimise the simulation time. The x-y-z planes are considered as a periodic boundary condition in the whole MD simulation. During the solid-solid interface in the FSSW process, the heat applied in each simulation is done using a Nose-Hoover thermostat at a specific temperature of 300 K and a time step of 1 fs. The initial velocity is set to obey the Gaussian distribution for Al, Cu, and C atoms.

3. Results and discussions

3.1. Temperature and axial force

Figs. 2 (a) and (b) illustrate the frictional heat generated during the Al-Cu welded samples without and with GL, respectively. The temperature generation for sample S_{2500} (527.64 ^{0}C) is lower than for sample $S_{GL\text{-}2500}$ (439.76 ^{0}C). The decrease in temperature is due to the presence of a GL. Since graphene is a high thermally conductive material, it absorbs the heat generated during the welding process. Fig. 2 (c) depicts, with an increase in ω, the frictional heat generation increases with an increase in temperature at the weld NZ [12]. However, the samples with GL observed less temperature than the samples without GL, as shown in Fig. 2 (c). The temperature generation during the FSSW has a direct impact on the axial load experienced by the tool. Figs. 2 (d) and (e) show the variation of axial force for different weld samples. As shown in Fig. 2 (d), the force plot has been divided into two sections. Initially, the increased force is due to tool plunging and constant fluctuations in force, which is due to the dwelling period. The welding process experiences a high amount of axial force when plunging into the Cu sheet and whereas the force slightly reduces when it enters into the Al sheets. The results show that with an increase in ω, the axial force decreases. The average axial force values for the samples S_{500}, $S_{1500,}$ and S_{2500} are 740.78 N, 582.73 N, and 368.81 N, respectively. In higher ω, frictional heat generation is higher, resulting in a decrease in axial force [11]. Fig. 2 (e) illustrates the variation of axial force in the welded samples with GL. The existance of GL where the tool penetrates into the work piece exerting a high axial load due to the presence of harder material at the weld interface. Because of this, the variation in tool plunging stage cannot be observed effectively. The average axial force for the samples $S_{GL\text{-}500}$, $S_{GL\text{-}1500,}$ and $S_{GL\text{-}2500}$, is 1038.73 N, 837.75 N, and 712.09 N, respectively. The temperature and axial force that has been acquired from the experimental FSSW process, is used to perform the MD simulations as discussed in later section.

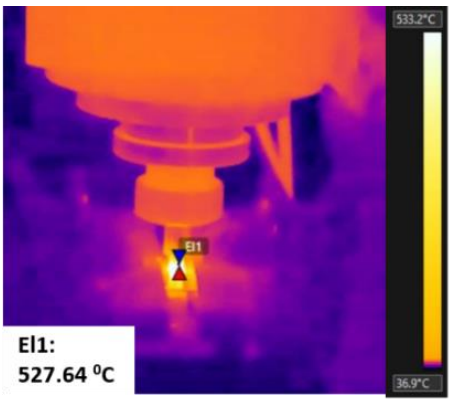

(a)

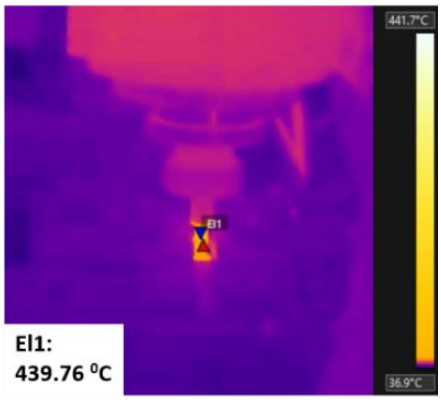

(b)

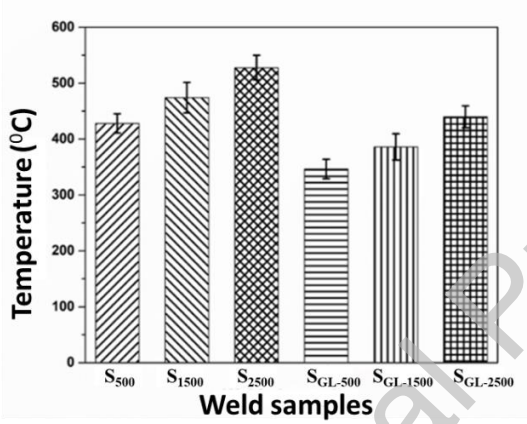

(c)

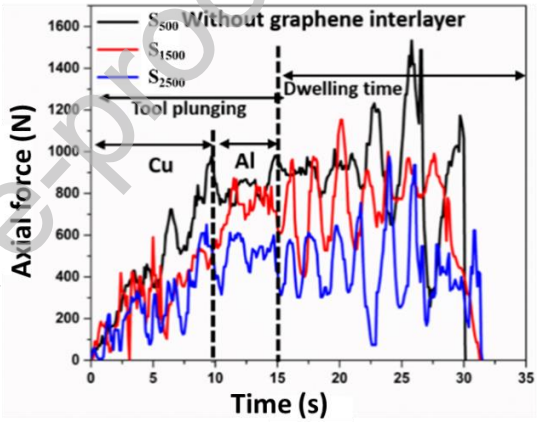

(d)

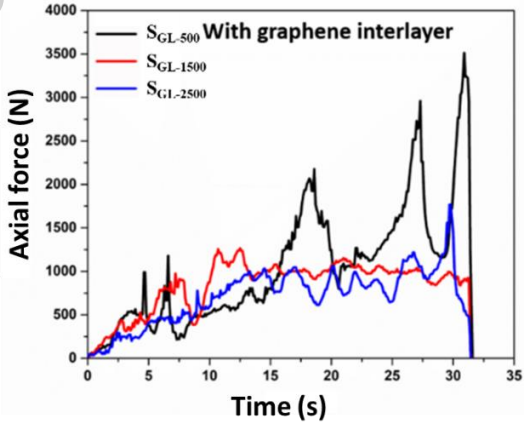

(e)

Fig. 2. Thermal imaging camera data for the welded samples: (a) $S_{2500,}$ (b) $S_{GL\text{-}2500,}$ and (c) variation of temperature with process parameters, variation of axial force, (d) without GL and (e) with GL

3.2. Tensile and IMC analyses

A monotonic tensile test is performed to analyze the possible impact of GL on the welded joints. Fig. 3 (a) presents the tensile load (P) – displacement (Δ) curves of the FSSW of Al-Cu with and without GL. Qualitatively, $P - \Delta$ curves are observed: the displacement for samples without GL, S_{500} and S_{2500} are nearly about ~ 2 mm, whereas sample S_{1500} is ~ 1.4 mm. However, it exhibits a higher tensile load. The Δ for the samples with GL, $S_{GL\text{-}500,}$ and $S_{GL\text{-}2500,}$ were observed ~ 1.15 mm, and sample $S_{GL\text{-}1500}$, has a higher displacement of ~ 2.3 mm than all other samples. Irrespective of Δ, S_{1500} found a higher joint efficiency of 66.39 % to base Al than S_{500} and S_{2500}. At the same time, $S_{GL\text{-}1500}$, exhibited a higher tensile load among all other samples with a joint efficiency of 84.28 %. Both with and without GL, the intermediate process parameter ω of 1500 rpm exhibits higher tensile load due to the optimal frictional heat generation that results in good material mixing and minimization of IMC formation. Fig. 3 (b) illustrates the failure morphology where it can be noticed that for a lower Δ, shear failure occurs in the samples. At a higher Δ, the samples experience a discontinuous hook displacement of Al and Cu. The macrostructure of facture surface of samples S_{1500} and $S_{GL\text{-}1500}$ are depicted in Fig. 3 (b). The Al content in the interface varies for samples with and without GL. Due to the diffusion of graphene in the Al matrix, sample $S_{GL\text{-}1500}$ exhibits high Al material over the Cu. The sample S_{1500} exhibits shear failure and observes a dimple over the fracture surface. The sample $S_{GL\text{-}1500}$ exhibits ductile failure leaving cleavages and dimples on the fracture surface.

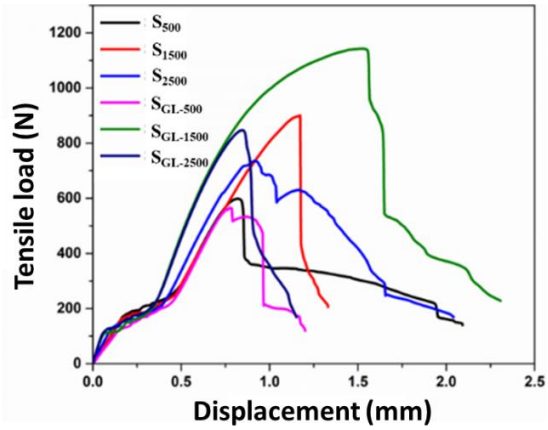

(a)

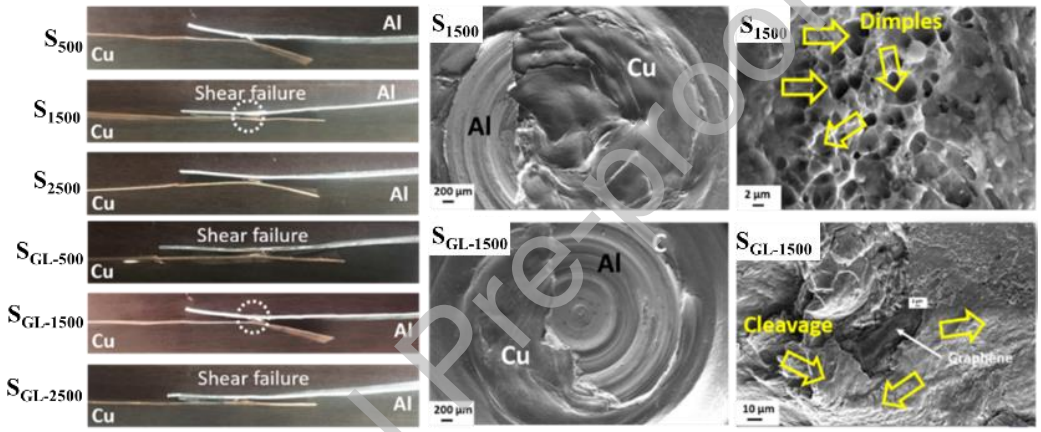

(b)

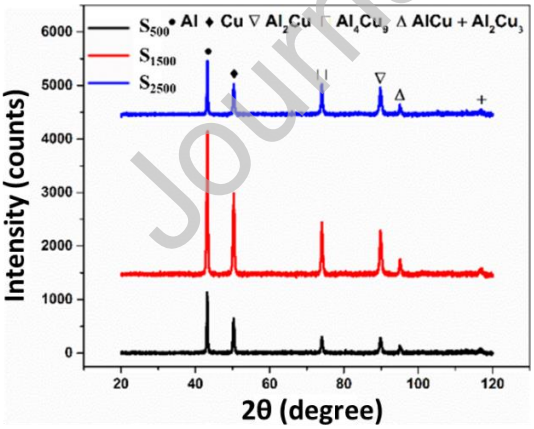

(c)

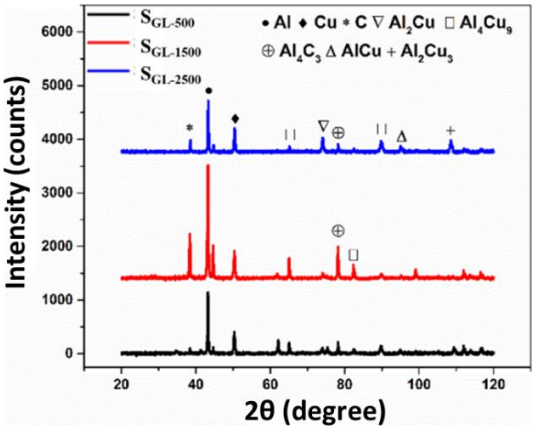

(d)

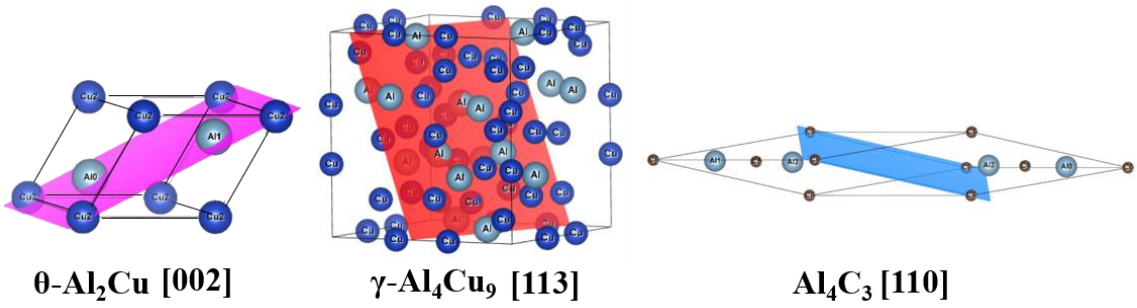

(e)

Fig. 3. (a) Variation of tensile load, (b) fracture morphology of all the FSSW joint, XRD analysis of (c) without GL, (d) with GL and (e) crystal structures of major IMCs along with the slip plains

Figs. 3 (c) and (d) describe the formation of IMC at particular 2θ angles. Generally, the difference in the formation of IMCs among the samples is due to variation in temperature generation [37] and plastic deformation [38]. Among the samples without a GL, two major and two minor IMCs are found, i.e., Al_2Cu, Al_4Cu_9, and AlCu, Al_2Cu_3, respectively. Fig. 3 (c) shows S_{1500} observed with a higher intensity of Cu-rich IMCs γ-Al_4Cu_9 (113) and brittle θ-Al_2Cu (002) IMC peaks compared to other S_{500} and S_{2500}. Fig. 3 (d) depicts the sample $S_{GL\text{-}1500}$ observed the γ-Al_4Cu_9 and Al_4C_3 as the two main IMCs among the welded samples with GL. Fig. 3 (e) illustrates the crystal structure of major IMCs formed during the joining process. Different IMCs can be distinguished from each other based on their shapes, sizes, and lattice planes in high resolution transmission microscopy images, as described in later sections.

The tensile properties of Al-Cu FSSW mainly depend on the generated temperature and axial load conditions. The variation in the process parameters to obtain a optimum heat generation and stirring action in the FSSW, intensifies the material mixing, resulting in a greater surface contact area and shorter diffusion path in the weldments [39]. The IMC formation at the interface is also responsible for the tensile load of a weld joint. During FSSW, higher densities of vacancies are developed in the Al-Cu weld interface, which enhances the kinetics of diffusion and results in the formation of IMCs [40]. However, S_{1500} with a higher intensity of Al_4Cu_9 exhibits a higher tensile load, and the presence of Al_2Cu IMC results in shear failure among the without GL samples [41]. The fracture occurs near the boundary of Al_2Cu, and AlCu attributes the shear

failure in sample S_{1500}. The shear failure occurs due to the different lattice structures of Al_2Cu (tetragonal) and AlCu (either monoclinic, orthorhombic) IMCs [41]. However, a maximum tensile load in sample $S_{GL\text{-}1500}$ is observed compared to all the six welded samples due to the formation of rich Al_4C_3 and Al_4Cu_9 IMCs. As mentioned earlier, Al_4Cu_9 resists the crack propagation, but this would not reduce Al-rich IMC. The restraining effect of Al_4C_3 in the Al matrix reduces the Al grain growth and Al-rich IMC, i.e., Al_2Cu and AlCu formation during the welding process [42]. Hence, these conditions lead to improved tensile load for sample $S_{GL\text{-}1500}$. The thickness of Al_4Cu_9 is more significant than the Al_2Cu as the crystal structure is more extensive for Al_4Cu_9, as shown in Fig. 3 (e). The coherence between the Al_4Cu_9 and Al-Cu matrix is much better than the Al_2Cu and AlCu. The cohesive nature of Al_4Cu_9 resists the crack propagation in the weld zone, which leads to a better tensile load. The increase in diffusivity of Al is due to severe plastic deformation and lesser atomic size of Cu, which facilitate the Al atoms to penetrate the Cu-matrix, resulting in the formation of γ-Al_4Cu_9 [21,43]. The penetration of Cu into Al is less, which might have led to the formation of θ-Al_2Cu at the interface. For a higher Δ, as depicted in Fig. 3 (a), the samples S_{1500} and $S_{GL\text{-}1500}$ experience a discontinuous hook displacement of Al and Cu, which exhibits a shear failure with dimples and a ductile failure leaving cleavages and dimples on the fractured surface, respectively. In addition, as shown in Fig. 2 (e), at lower ω, a large amount of axial force is generated due to more number of nucleation sites at the weld interface. Wang et al. [44] stated that the dispersion of harder particles like graphene into the ductile matrix causes dislocations to prevent void formation. The dislocations accumulated at the Al-Cu interface lead to an increase in work hardening, and thus, the maximum tensile load is observed compared to samples without a GL [44]. Further, it has been observed that dislocations are activated and accumulated near the interface between Al and Cu, increasing plastic strain. It confirms severe plastic deformation and diffusion of carbon into the Al-Cu matrix from more carbon-based IMCs.

3.3. TEM analysis

Figs. 4 and 5 illustrate TEM images of Al-Cu weld interface without and with GL, respectively. From Fig. 4 (a), it has been observed that dislocations are activated and accumulated near the interface between Al and Cu. Fig. 4 (b) illustrates the formation of eutectic Al_2Cu and Al_4Cu_9 IMC near the Al and Cu-side, respectively, during the FSSW condition. As Al_2Cu has a smaller

crystal structure than Al_4Cu_9, the size of the IMCs can be distinguished in the microscope images as shown in Fig. 4 (b). The Al_4Cu_9 is formed due to the localized mixing of Al and Cu in a solid state. Fig. 4 (c) illustrates that the twins are nucleated at the grain boundary and situated in the Cu-matrix [45]. As shown in Fig. 4 (d), the TEM image depicts high-density edge dislocations of size 0.79 nm and are prevalent along the (001) slip plane with FCC grains, indicating that the dislocations are nucleated. A selective area diffraction (SAED) pattern shown in Fig. 4 (e) suggests the interface has FCC structures corresponding to Cu atoms.

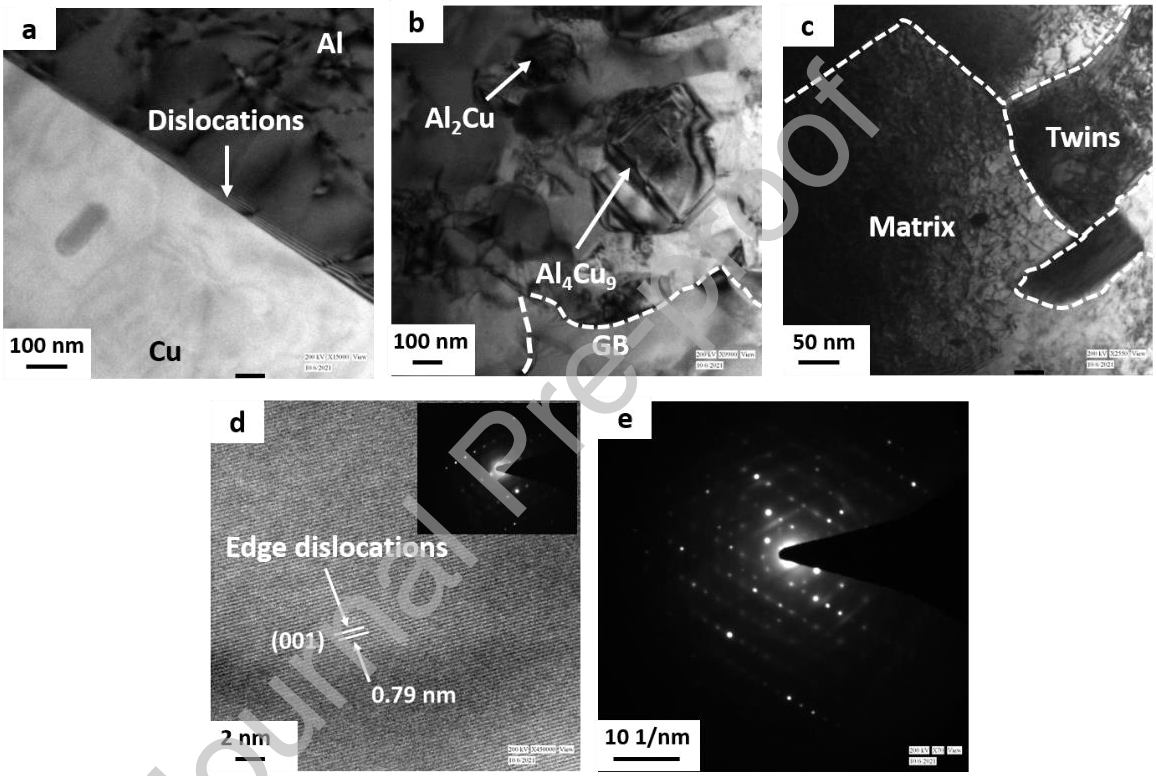

Fig. 4. TEM images of (a) Al-Cu interface with dislocations, (b) Al_2Cu, and Al_4Cu_9 IMCs pinned into the Al matrix, (c) Twin formation in Cu matrix, and (d-e) HRTEM image along with SAED patterns identifying FCC grains

The interaction of Al and carbon at a frictional heat, i.e., 300 ^{0}C - 600 ^{0}C range, results in the formation of Al_4C_3 IMC. In addition, during the formation of Al_4C_3, it consumes available Al leading to enhanced interfacial bonding between Al and Cu [46]. However, Fig. 3 (d) depicts the XRD plot of FSSW of Al-Cu with and without GL, where the sample $S_{GL\text{-}1500}$ depicts the formation of more Al_4C_3 IMC and less Al_2Cu IMC compared to other welded samples. This is

due to an initial stirring action of the FSSW tool fragments the graphene layer and disperse the particles into the Al-matrix. Accordingly, the TEM bright-field characterization is carried out at the weld interface and the images are shown in Fig. 5 (a-d). Most of the C atoms are distributed along the Al grain boundaries, schematically shown in Fig. 1 and validated with the TEM analysis as shown in Fig. 5. However, in Al microstructure, few atoms are scattered due to grain boundary migration. Additionally, the presence of GL at the interface, increases the more nucleation sites ascompared to samples without GL. This results in severe plastic deformation and higher dislocation density, i.e., accumulation of dislocations in the weld zone, as depicted in Fig. 5 (c), and thus advantageous to improve strength in sample $S_{GL\text{-}1500}$. The carbon usually shows less contrast present near the grain boundary of Al, as shown in Fig. 5 (a-b). The Al_4C_3 IMC is formed with sufficient heat and the required amount of available Al at the weld interface [47]. However, the Al_4C_3 IMCin the Al-matrix is illustrated in Fig. 5 (b-c). Researchers have stated that Al_4C_3 is formed during the composite of Al and graphene. They found that a rod-like structure is present within the Al-matrix, and was further analyzed using HRTEM [48]. Fig. 5 (d) depicts the formation of thinner/high-density twins in the Cu-matrix. Moreover, higher twin density is observed for the sample with GL compared to without graphene samples. The details of formation of twins is explained in later section. The HRTEM images illustrate the size of the dislocation of 0.83 nm along the [003] slip plane, as shown in Fig. 5 (e). They indicate the presence of more nucleation sites than sample S_{1500}. Fig. 5 (f) illustrates the SAED patterns over the selected area showing an amorphous ring with crystalline (FCC) structure, concluding the presence of Al_4C_3 IMC [46,49,50].

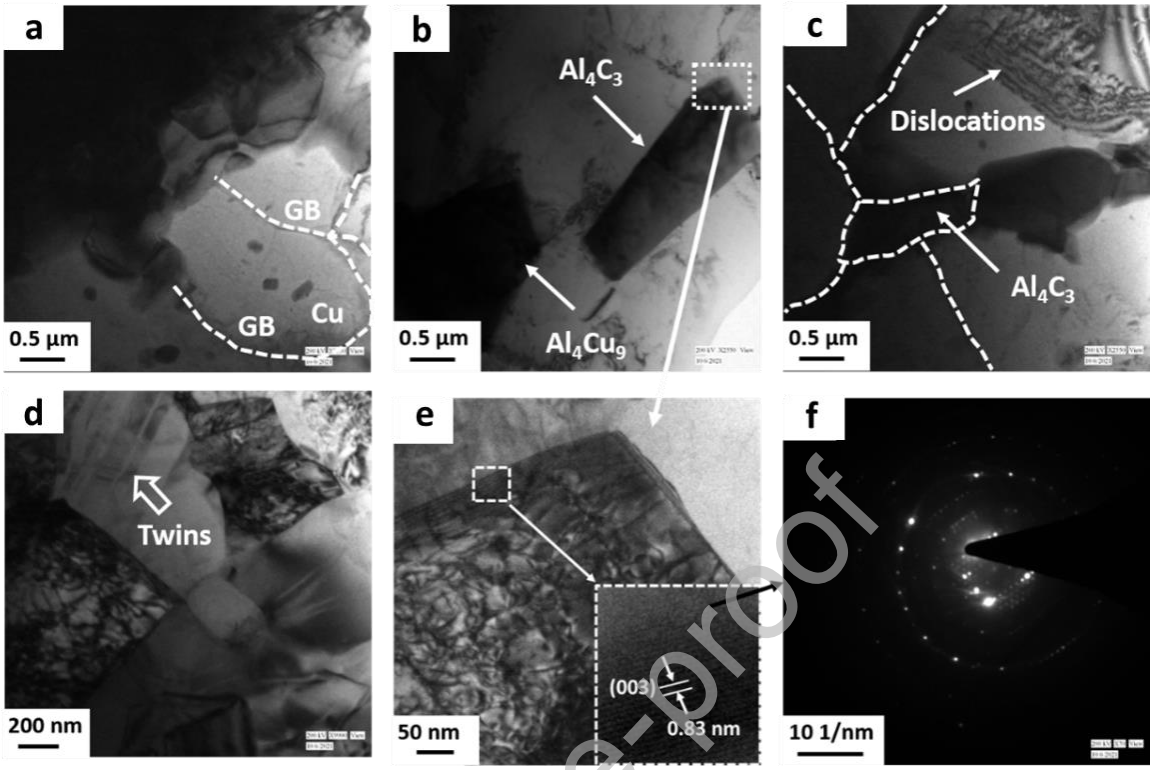

Fig. 5. TEM images of Al-Cu with graphene as interlayer (a) illustrate the grain boundaries and C particles, (b) formation of high dislocation density and Al_4C_3, (c) rod-like structures of Al_4C_3, (d) Twins formation, and (e-f) HRTEM and SAED patterns for the Al_4C_3 IMC

3.4. Diffusion and twins formation phenomenon

MD simulations are carried out to measure the diffusion coefficients of Al, Cu, and C and twin formation under FSSW conditions. Figs. 6 (a-b) illustrate the MD simulation box of Al-Cu without and with GL, respectively. It has been observed that the graphene atoms are in hexagonal ring structures which defines graphene and stacked between Al and Cu atoms as shown in Fig. 6 (b). MD simulations are performed on welded samples with maximum tensile load, which consider as optimised process parameter condition to analyze the diffusion mechanisms in FSSW of Al-Cu joining. The MD simulations are performed with FSSW process conditions, i.e., a gradual increase in temperature at a rate of 10 K/ps (picosecond) from 300 K to the maximum temperature of 747.15 K and 658.89 K for samples S_{1500} and $S_{GL\text{-}1500}$, respectively. A canonical ensemble NVT mole (N), volume (V), and temperature (T) has been used. The axial load from the experiment is converted into compressive strain rates. Axial stress is determined

by dividing the axial load with the tool's area of contact on the sample. The compressive strain rate is then found by dividing the axial stress by the elastic modulus of the sample. Accordingly the compressive starin rates are 1.24 E-3 s^{-1} and 2.47 E-3 s^{-1} for the samples S_{1500} and $S_{GL\text{-}1500}$, respectively. The strain values are fed into the MD simulation with the increasing temperature. After that, the whole system is cooled to 300 K at a cooling rate of 10 K/ps. Further, the output obtained from the simulation is analyzed using a modifier adaptive common neighbour analysis (a-CAN) in OVITO software. The a-CAN distinguishes various crystalline structure formations during FSSW of Al-Cu with and without GL [51].

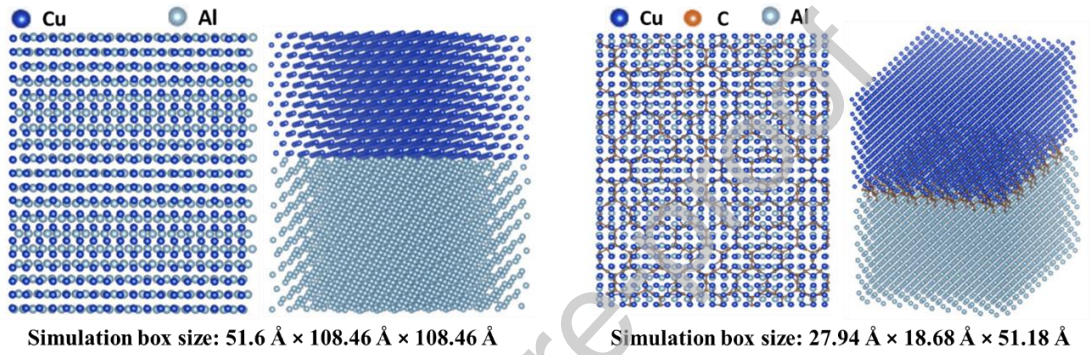

(a) (b)

Fig. 6. Initial orientation of (a) Al and Cu atoms without GL, and (b) Al and Cu atoms with GL

The mean square displacement (MSD) of Al-Cu and C atoms are calculated using LAMMPS software. This has been done to measure the movement of atoms during FSSW conditions. Every 1000 steps, MSD data is collected to determine the mutual diffusion of atoms at the interface. Equation 1 calculates the MSD [52].

$$MSD = \langle |X_i(t + t') - X_i(t)|^2 \rangle, \qquad \text{Eq. (1)}$$

where $X_i(t)$ is the instantaneous particle at the i^{th} position, t is the lag time, and $\langle - \rangle$ is the ensemble average.

Al and Cu diffusion coefficients (D) are calculated using the Einstein equation in accordance with their positions over time, as shown in Equation 2 [52].

$$D = \frac{1}{6}\lim_{t\to\infty}\frac{dMSD}{dt} \qquad \text{Eq. (2)}$$

Initially, FCC structured Al and Cu atoms are placed one over the other, and the FSSW condition is applied to the system. The MSD of FCC metals occurs due to a coherent interface. Fig. 7 (a) illustrates the interaction between the Al-Cu interface, and the MSD curves are plotted using the values obtained from the system. The diffusivity of atoms is determined by measuring the change in the slope of the MSD curves. The movement of atoms takes place only when there is a change in slope of MSD curve is non-zero, where the transfer of energy takes place due to interactions of Al and Cu atoms. The the diffusion coefficient of Al (D_{al}) and the diffusion coefficient of Cu (D_{cu}) values were obtained from the simulation results based on the calculation represented in equation 2, accordingly the D_{Al} and D_{Cu} are 7.37 E-8 cm^2/sec and 3.24 E-8 cm^2/sec, respectively. In addition, the presence of a graphene layer at the Al-Cu interface during the FSSW condition decreased the diffusivity of Al and Cu [21]. Fig. 7 (b) shows, the D_{Al}, D_{Cu}, and D_C is calculated to be 3.22 E-8 cm^2/sec, 1.125 E-8 cm^2/sec, and 0.195 E-8 cm^2/sec, respectively. Moreover, the presence of graphene initiates the formation of the rod-like Al_4C_3 structures towards the Al matrix, as illustrated in Fig. 7 (b). Hence the diffusivity of Al and Cu is decreased by 43.69 % and 34.72 %, respectively. The reduction in diffusivity results in the lesser Al-rich IMC formation.

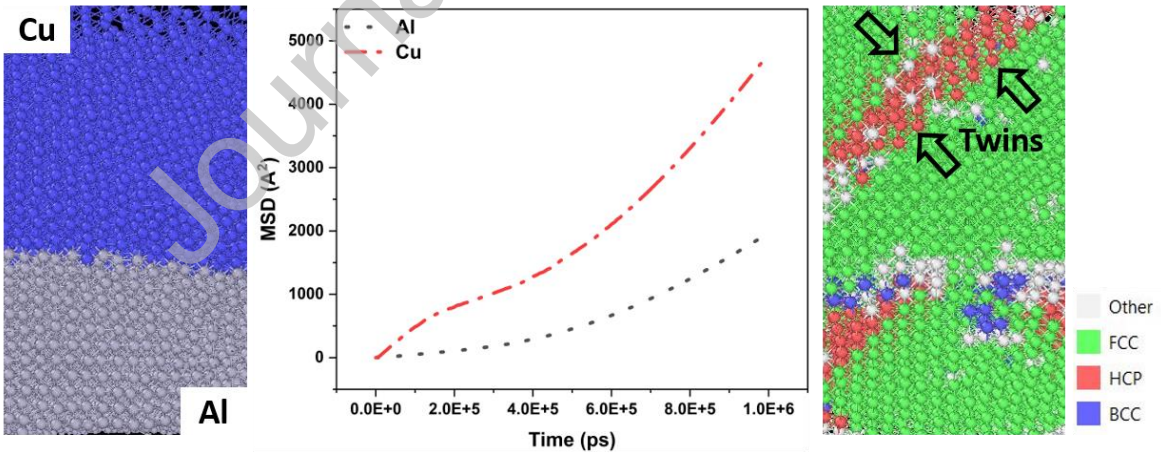

(a)

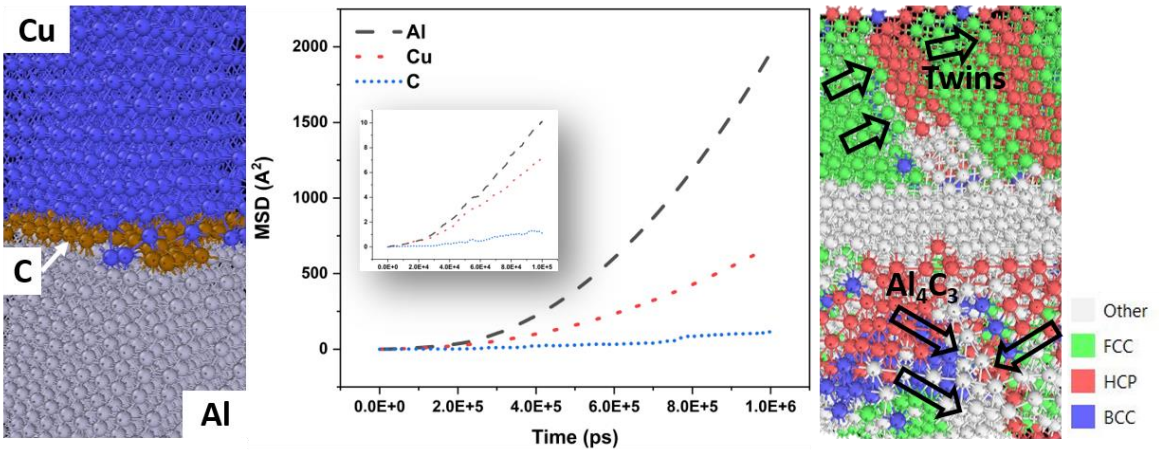

(b)

Fig. 7. (a) Interfacial bonding of Al and Cu along with the MSD curves of Al and Cu and identification of twin and IMC formations at the Al-Cu matrix for the sample S_{1500} and (b) interfacial bonding with graphene as interlayer along with MSD curves for Al, Cu, and C and formation of thin twin and Al_4C_3 IMC in the Cu and Al matrix, for the sample $S_{GL\text{-}1500}$ respectively.

The FCC material like Cu with lower stacking fault energy (SFE) has a tendency of twinning occurs in the metal matrix [53]. The twin boundary density increases with a decrease in twin thickness. Fig. 7 (a) shows the thicker twin boundary in sample S_{1500} compared to sample $S_{GL\text{-}1500}$. Whereas sample $S_{GL\text{-}1500}$ has a high twin boundary density, as depicted in Fig. 7 (b). However, the number of twin grains increases with an increase in deformation strain and eventually saturates once the strain exceeds an accumulated capacity during the welding process. The presence of high dislocation density in sample $S_{GL\text{-}1500}$ resists the twin growth, leading to thinner twins towards the Cu-side of the weld interface [54–56]. Moreover, the presence of dislocations in the Al-Cu metal matrix hinders the expansion of twins; hence the thickness of twins is smaller in sample $S_{GL\text{-}1500}$.

3.5. Electrical resistivity

3.5.1 Experimental study

Initially, the electrical resistivity of the FSSW joints decreases for ω from 500 rpm to 1500 rpm and increases for 2500 rpm in both with and without GL conditions, as shown in Fig. 8 (a). At

lower ω, very less amount of heat is generated due to the presence of Cu sheet placed over the Al sheet as depicted in Fig. 1. This kind of weld configuration conducts more heat rapidly, resulting in a lack of frictional heat at the joint interface. The variation in heat generation will effect the electrical resisitivity of the weld samples. Based on that, Fig. 8 (a) shows samples S_{1500} and $S_{GL-1500}$ exhibit lower electrical resistivity among other welded samples respective to with and without GL. Despite this, the welded samples with other process parameter conditions have higher electrical resistivity than the base material due to the formation of Al-rich IMC at the weld interface. Moreover, the electrical resisitivity for samples S_{1500} and $S_{GL-1500}$ are found to be 73.3 % and 26.2 % high resistive than Al base material. At lower ω leads to poor material mixing, which intends to increase in electrical resisitivity. In contrast, at higher ω, the weldments experience excess plastic deformation, increasing the number of electron-scattering dislocations in the weld interface, which leads to increase in electrical resistivity of the weld samples. In addition, the electrical resistivity of the weld joints depends on the formation of Al-rich IMCs at the interface and variation in the grain size due to change in process parameters. Previously, the IMC study has been done by using XRD analyses and the grain size of Al for samples S_{1500} and $S_{GL-1500}$ are analyzed using EBSD analyses. Fig. 8 (a) shows a larger elongated grain size of 20.21 μm at the NZ for sample S_{1500}. In contrast, sample $S_{GL-1500}$ had a smaller grain size of 4.07 μm at the NZ, as shown in Fig. 8 (b). The energy dispersive X-ray analysis (EDAX) analysis is performed to confirm the impinging of C particles near the grain boundary, as illustrated in Fig. 8 (b).

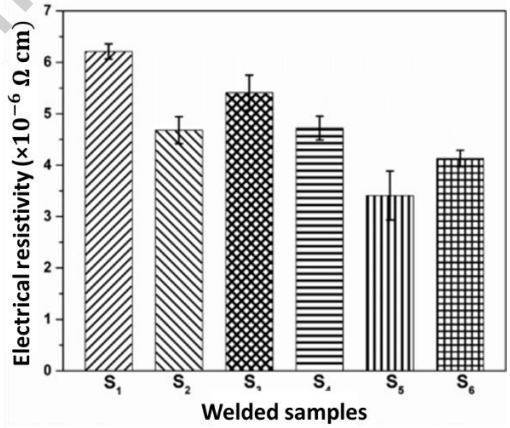

(a)

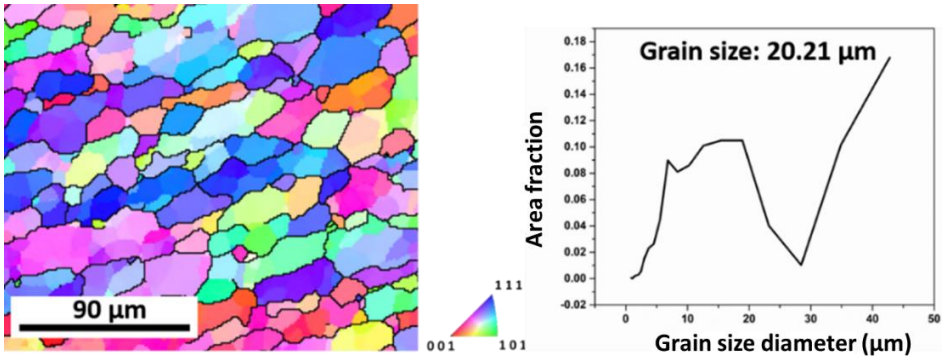

(b)

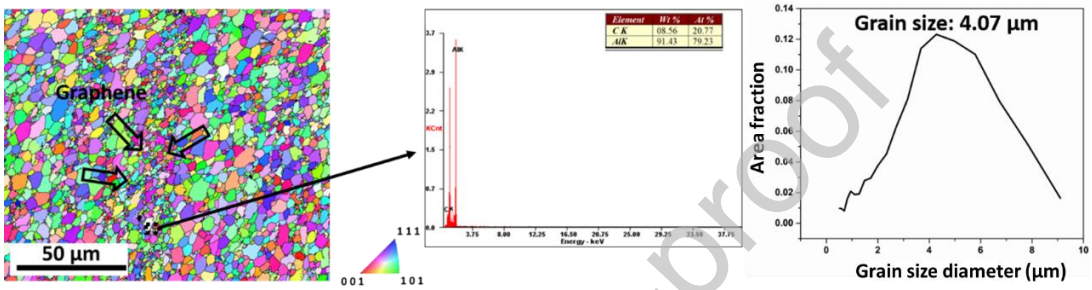

(c)

Fig. 8. (a) Variation in the electrical resistivity with different process parameters, EBSD analyses of Al at the weld nugget zone of samples (b) S_{1500} and (c) $S_{GL-1500}$ and also showing the presence of carbon near the grain boundaries.

Generally, the tensile load and σ of welded samples show a trade-off behaviour [49]. The samples with lower tensile load should exhibit higher σ. Accordingly, it is expected that the samples without GL would have lower electrical resistivity. However, it has been found that the samples with GL had a lower electrical resistivity than other samples. The presence of GL increases the number of nucleation sites during welding, which results in a decrease in brittle IMC formation. Accordingly, the electrical resisitivity of sample $S_{GL-1500}$, as shown in Fig. 8 is decreased mainly due to the formation of Al_4C_3 (110) IMC towards Al-matrix. This inhibits the formation of detrimental, non-conductive Al-rich IMC during the FSSW. The presence of a significant amount of Al_4C_3 IMCs actively participates in electron mobility. However, the electron mobility of graphene is much higher, which is in the range of 0.5 m^2/V.s – 2.5 m^2/V.s than Al base metal (0.0013 m^2/V.s) [57]. The decreased electrical resistivity for the sample with GL is due to a decrease in the formation of Al-rich IMCs in the weld NZ. In addition to the type of IMC formation, grain boundary formation also has significant importance in variation in σ. As

mentioned earlier, the presence of graphene increases the nucleation sites, and the pinning of carbon near grain boundaries, as shown in Fig. 5 (a), inhibits grain growth, i.e., hindering grain boundary migration. Hence, less grain size is obtained for sample $S_{GL\text{-}1500}$ as compared to S_{1500}. Increasing the grain boundary density reduces the electrical resistivity of polycrystalline grains [58,59]. Due to the presence of polycrystalline material within the Al grains, i.e., graphene particles, the dislocations within the grains are lessened, resulting in an increase in electron flow, which in turn decreases electrical resisitivity.

3.2.2 Simulation study

The Nernst-Einstein (NE) equation measures the σ from the atomic diffusion coefficient. The implementation of NE required individual atomic diffusivity, and no atomic interactions are needed. Hence a new model, i.e., cluster Nernst-Einstein (cNE) [33] has been introduced for a system with interactions between the atoms. The σ of a given system is computed using a cNE, as mentioned in Equation 3.

$$\sigma_{cNE} = \frac{e^2}{V\, k_B T} \sum_{i=0}^{n} \sum_{j=0}^{n} N_{ij} z_{ij}^2 D_{ij} \qquad \text{Eq. (3)}$$

Where σ_{cNE} is the cluster-NE conductivity, e is the charge, k_B is a Boltzmann constant, V is volume, T is temperature, D is a diffusion coefficient of atoms, z is a charge of the atoms, and N is the number of cations and anions present in the system.

However, σ_{cNE} has a direct dependency on diffusion coefficients and concentrations of elements. The cNE model is able to detect the in-situ σ_{cNE} during the FSSW condition. Fig. 9 depicts the σ_{cNE} of sample S_{1500} and $S_{GL\text{-}1500}$ and observed a linear increase in conductivity according to the change in time. Among them, sample $S_{GL\text{-}1500}$ exhibits a 56.25 % higher σ_{cNE} compared to sample S_{1500}. The increase in σ_{cNE} is further investigated with the XPS analysis to understand the atoms interaction during FSSW it has been detailed more in the supplementary document. Fig. 9 shows the mechanism of cNE for Al-Cu and Al-Cu-C interactions. In the welded sample with Al-Cu, the interactions between Al-Al or Al-Cu are made with Cu/Al to form a cluster, and then this cluster will not interact with any other individual atoms or cluster. Hence, free-moving

clusters are available with Al-Cu to transport the electrons, similar to actual experimentation conditions [33].

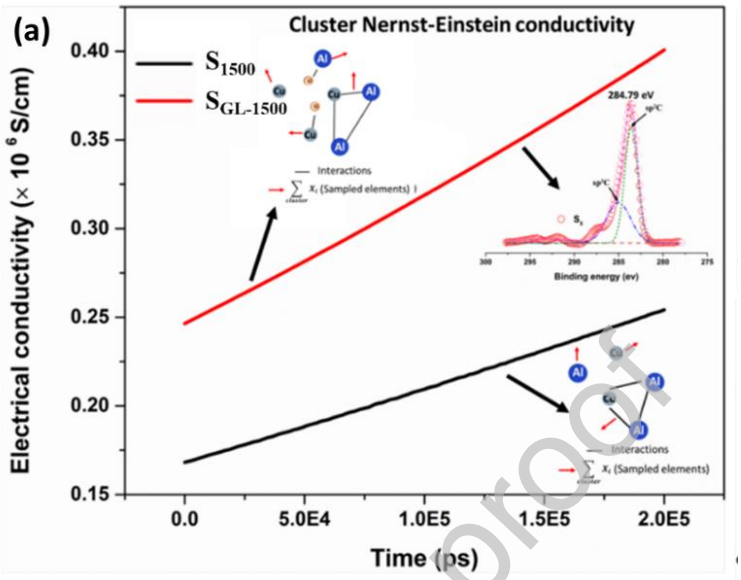

Fig. 9. The σ plot with an increase in the cooling time illustrating the cluster Nernst-Einstein conductivity mechanism

The interactions between Al-Cu-C are further analyzed, as shown in Fig. 8. Generally, the binding energy has a direct proportionality with temperature. As mentioned earlier, the heat generation is less for sample $S_{GL-1500}$ compared to sample S_{1500}. The σ obtained from the MD simulation illustrates an increase in time, i.e., cooling time. In addition, an increased σ in sample $S_{GL-1500}$ is likely due to an increase in nucleation sites at the weld interface caused by the presence of carbon atoms towards Al-side. For FCC alloys, decreased temperature and an increase in strain rate also lead to increased twin nucleation. Moreover, twin growth is controlled by the deformation strain rate and temperature [61,62]. Twin growth occurs when two dislocations cross-slip onto successive (001) and (003) planes for the samples with and without GL, as depicted in Figs. 3 (c) and 3 (e), respectively. Experimentally, the increase in nucleation with the presence of graphene increases the deformation strain increasing the joint strength. Hence, sample S_{1500} exhibits a lower tensile load. Fig. 7 (a), thicker twin boundaries are depicted in sample S_{1500} compared to sample $S_{GL-1500}$. However, the number of twin grains increases with an increase in deformation strain and eventually saturates once the strain exceeds an accumulated capacity during the welding process. The presence of high dislocation density in sample $S_{GL-1500}$

resists the twin growth, leading to thinner twins towards the Cu-side of the weld interface [54–56]. Moreover, the presence of dislocations in the Al-Cu metal matrix hinders the expansion of twins; hence the thickness of twins is smaller in sample $S_{GL\text{-}1500}$. Hence, it concludes that sample $S_{GL\text{-}1500}$ has a high twin boundary density, resulting in higher tensile load and σ [63].

4. Conclusion

A study of the effect of graphene on tensile load and electrical resistivity is conducted on FSSW dissimilar Cu-Al joints. TEM, EBSD analyses, and MD simulations are performed to gain insights into the welding process. The maximum tensile load is achieved for a graphene-induced Al-Cu dissimilar FSSW. The presence of graphene increases the nucleation site at the interface, which causes severe plastic deformation resulting in smaller grain size and increased mechanical strength. Further, the fractographic results for the samples with and without GL show the shear mode of failure and quasi-cleavage fractures, respectively, in the loading direction. Moreover, in FSSW of Al-Cu, the interfacial microstructure analyses revealed that the formation of Al_2Cu and AlCu deteriorates the joint strength in the sample without a GL. In contrast, the presence of graphene inhibits the formation of Al_2Cu, where C consumes the available Al to form Al_4C_3. The Al_4C_3 IMC is beneficial to reduce the formation of brittle IMCs at the weld interface. The presence of Al_4C_3 IMC decreases the electrical resistivity of the weld sample. Additionally, MD simulations provide insight into the in situ diffusion of atoms, where Al is profoundly diffused into the Cu atoms to form Al-rich IMCs at the interface. The presence of graphene decreases the diffusion coefficient of Al by 43.69 %, which illustrates the reduction in the formation of Al-rich IMCs. The results show that the FSSW for Al-Cu joints can be simply performed over Li-ion batteries.

Declaration of Competing Interest

The authors declare that they have no known competing financial interests or personal relationships that could have appeared to influence the work reported in this paper.

Acknowledgments

The MD simulation is carried out in this work by using the Supercomputing facility of IIT Kharagpur established under National Supercomputing Mission (NSM), Government of India and supported by Centre for Development of Advanced Computing (CDAC), Pune.

Data availability statement

The datasets generated during and/or analysed during the current study are available from the corresponding author on reasonable request.

References

[1] W. Sierzchula, S. Bakker, K. Maat, B. Van Wee, Technological diversity of emerging eco-innovations: A case study of the automobile industry, J. Clean. Prod. 37 (2012) 211–220. https://doi.org/10.1016/j.jclepro.2012.07.011.

[2] T. Placke, R. Kloepsch, S. Dühnen, M. Winter, Lithium ion, lithium metal, and alternative rechargeable battery technologies: the odyssey for high energy density, J. Solid State Electrochem. 21 (2017) 1939–1964. https://doi.org/10.1007/s10008-017-3610-7.

[3] B. Li, F. Dai, Q. Xiao, L. Yang, J. Shen, C. Zhang, M. Cai, Activated Carbon from Biomass Transfer for High-Energy Density Lithium-Ion Supercapacitors, Adv. Energy Mater. 6 (2016) 1–6. https://doi.org/10.1002/aenm.201600802.

[4] O. Mypati, D. Mishra, S. Sahu, S.K. Pal, P. Srirangam, A Study on Electrical and Electrochemical Characteristics of Friction Stir Welded Lithium-Ion Battery Tabs for Electric Vehicles, J. Electron. Mater. (2019). https://doi.org/10.1007/s11664-019-07711-8.

[5] O. Mypati, S.K. Pal, P. Srirangam, A Study on Electrical Conductivity of Micro Friction Stir-Welded Dissimilar Sheets for Hybrid Electric Vehicles (HEVs), Springer International Publishing, n.d. https://doi.org/10.1007/978-3-030-05861-6.

[6] A. Das, L. Dezhi, W. David, G. David, Joining Technologies for Automotive Battery Systems Manufacturing, World Electr. Veh. J. 9 (2018) 1–13. https://doi.org/10.3390/wevj9020022.

[7] J. Jiang, P. Nie, B. Ding, Y. Zhang, G. Xu, L. Wu, H. Dou, X. Zhang, Highly stable

lithium ion capacitor enabled by hierarchical polyimide derived carbon microspheres combined with 3D current collectors, J. Mater. Chem. A. 5 (2017) 23283–23291. https://doi.org/10.1039/c7ta05972h.

[8] W. Giurlani, L. Sergi, E. Crestini, N. Calisi, F. Poli, F. Soavi, M. Innocenti, Electrochemical stability of steel, Ti, and Cu current collectors in water-in-salt electrolyte for green batteries and supercapacitors, J. Solid State Electrochem. (2020). https://doi.org/10.1007/s10008-020-04853-2.

[9] L. Guo, D.B. Thornton, M.A. Koronfel, I.E.L. Stephens, M.P. Ryan, Degradation in lithium ion battery current collectors, 3 (2021) 32015. https://doi.org/10.1088/2515-7655/ac0c04.

[10] R.P. Mahto, S. Anishetty, A. Sarkar, O. Mypati, S.K. Pal, J.D. Majumdar, Interfacial Microstructural and Corrosion Characterizations of Friction Stir Welded AA6061-T6 and AISI304 Materials, Met. Mater. Int. (2018). https://doi.org/10.1007/s12540-018-00222-x.

[11] O. Mypati, A. Sadhu, S. Sahu, D. Mishra, Enhancement of joint strength in friction stir lap welding between AA6061 and AISI 304 by adding diffusive coating agents, (2019) 1–14. https://doi.org/10.1177/0954405419838379.

[12] S. Sahu, O. Mypati, S.K. Pal, M. Shome, P. Srirangam, Effect of weld parameters on joint quality in friction stir welding of Mg alloy to DP steel dissimilar materials, CIRP J. Manuf. Sci. Technol. 35 (2021) 502–516. https://doi.org/10.1016/j.cirpj.2021.06.012.

[13] P. Kah, C. Vimalraj, J. Martikainen, R. Suoranta, Factors influencing Al-Cu weld properties by intermetallic compound formation, Int. J. Mech. Mater. Eng. 10 (2015). https://doi.org/10.1186/s40712-015-0037-8.

[14] L.A. Cook, Aluminum-dissimilar metal joint and method of making same, US2790656, 1957.

[15] M. Asemabadi, M. Sedighi, M. Honarpisheh, Investigation of cold rolling influence on the mechanical properties of explosive-welded Al/Cu bimetal, Mater. Sci. Eng. A. 558 (2012) 144–149. https://doi.org/10.1016/j.msea.2012.07.102.

[16] N. Shen, A. Samanta, H. Ding, W.W. Cai, Simulating microstructure evolution of battery tabs during ultrasonic welding, J. Manuf. Process. 23 (2016) 306–314. https://doi.org/10.1016/j.jmapro.2016.04.005.

[17] R. Heideman, C. Johnson, S. Kou, Metallurgical analysis of Al/Cu friction stir spot welding, Sci. Technol. Weld. Join. 15 (2010) 597–604. https://doi.org/10.1179/136217110X12785889549985.

[18] M.J. Brand, P.A. Schmidt, M.F. Zaeh, A. Jossen, Welding techniques for battery cells and resulting electrical contact resistances, J. Energy Storage. 1 (2015) 7–14. https://doi.org/10.1016/j.est.2015.04.001.

[19] M. Shiraly, M. Shamanian, M.R. Toroghinejad, M.A. Jazani, Effect of Tool Rotation Rate on Microstructure and Mechanical Behavior of Friction Stir Spot-Welded Al/Cu Composite, J. Mater. Eng. Perform. 23 (2013) 413–420.

[20] M.P. Mubiayi, E.T. Akinlabi, Characterization of the intermetallic compounds in aluminium and copper friction stir spot welds, Mater. Today Proc. 4 (2017) 533–540. https://doi.org/10.1016/j.matpr.2017.01.054.

[21] O. Mypati, P.K. Polkampally, P.I. MD, S. Pal, P. Srirangam, Molecular dynamics simulation of atomic diffusion in friction stir spot welded Al to Cu joints, Mech. Adv. Mater. Struct. (2021). https://doi.org/10.1080/15376494.2021.1972188.

[22] A. Boucherit, S. Abdi, M. Aissani, B. Mehdi, K. Abib, R. Badji, Weldability, microstructure, and residual stress in Al/Cu and Cu/Al friction stir spot weld joints with Zn interlayer, Int. J. Adv. Manuf. Technol. 111 (2020) 1553–1569. https://doi.org/10.1007/s00170-020-06202-z.

[23] P.K. Sahu, S. Pal, S.K. Pal, Al/Cu Dissimilar Friction Stir Welding with Ni, Ti, and Zn Foil as the Interlayer for Flow Control, Enhancing Mechanical and Metallurgical Properties, Metall. Mater. Trans. A Phys. Metall. Mater. Sci. 48 (2017) 3300–3317. https://doi.org/10.1007/s11661-017-4093-y.

[24] A. Boucherit, M.N. Avettand-Fènoël, R. Taillard, Effect of a Zn interlayer on dissimilar

FSSW of Al and Cu, Mater. Des. 124 (2017) 87–99. https://doi.org/10.1016/j.matdes.2017.03.063.

[25] A. Sharma, V.M. Sharma, A. Gugaliya, P. Rai, S.K. Pal, J. Paul, Friction stir lap welding of AA6061 aluminium alloy with a graphene interlayer, Mater. Manuf. Process. 35 (2020) 258–269. https://doi.org/10.1080/10426914.2020.1718694.

[26] D. Jayabalakrishnan, M. Balasubramanian, Eccentric-weave FSW between Cu and AA 6061-T6 with reinforced Graphene nanoparticles, Mater. Manuf. Process. 33 (2018) 333–342. https://doi.org/10.1080/10426914.2017.1339323.

[27] M.H. Montazerian, M. Movahedi, M.R. Jondi, Effect of graphene and process parameters on mechanical performance and electrical resistance of aluminum to copper friction stir joint, Mater. Res. Express. 6 (2019) 46561. https://doi.org/10.1088/2053-1591/aafe1a.

[28] R. Li, H. Kang, Z. Chen, G. Fan, C. Zou, W. Wang, S. Zhang, Y. Lu, J. Jie, Z. Cao, T. Li, T. Wang, A promising structure for fabricating high strength and high electrical conductivity copper alloys, Sci. Rep. 6 (2016) 1–9. https://doi.org/10.1038/srep20799.

[29] S. Zhang, P. Huang, F. Wang, Graphene-boundary strengthening mechanism in Cu/graphene nanocomposites: A molecular dynamics simulation, Mater. Des. 190 (2020) 108555. https://doi.org/10.1016/j.matdes.2020.108555.

[30] S.D. Chen, A.K. Soh, F.J. Ke, Molecular dynamics modeling of diffusion bonding, Scr. Mater. 52 (2005) 1135–1140. https://doi.org/10.1016/j.scriptamat.2005.02.004.

[31] J.K. Chen, D. Farkas, W.T. Reynolds, Atomistic simulation of an f.c.c./b.c.c. interface in Ni-Cr alloys, Acta Mater. 45 (1997) 4415–4421. https://doi.org/10.1016/S1359-6454(97)00159-6.

[32] A. Mao, J. Zhang, S. Yao, A. Wang, W. Wang, Y. Li, C. Qiao, J. Xie, Y. Jia, The diffusion behaviors at the Cu-Al solid-liquid interface: A molecular dynamics study, Results Phys. 16 (2020). https://doi.org/10.1016/j.rinp.2020.102998.

[33] A. France-Lanord, J.C. Grossman, Correlations from Ion Pairing and the Nernst-Einstein Equation, Phys. Rev. Lett. 122 (2019) 136001.

https://doi.org/10.1103/PhysRevLett.122.136001.

[34] X. Zhang, Z. Chen, H. Chen, L. Xu, Comparative studies of thermal conductivity for bilayer graphene with different potential functions in molecular dynamic simulations, Results Phys. 22 (2021) 103894. https://doi.org/10.1016/j.rinp.2021.103894.

[35] K. Kanhaiya, S. Kim, W. Im, H. Heinz, Accurate simulation of surfaces and interfaces of ten FCC metals and steel using Lennard–Jones potentials, Npj Comput. Mater. 7 (2021) 1–15. https://doi.org/10.1038/s41524-020-00478-1.

[36] S. Kumar, Effect of applied force and atomic organization of copper on its adhesion to a graphene substrate, RSC Adv. 7 (2017) 25118–25131. https://doi.org/10.1039/c7ra01873h.

[37] C.T. Chi, C.G. Chao, T.F. Liu, C.H. Lee, Aluminum element effect for electron beam welding of similar and dissimilar magnesium-aluminum-zinc alloys, Scr. Mater. 56 (2007) 733–736. https://doi.org/10.1016/j.scriptamat.2007.01.028.

[38] P. Peng, K. Wang, W. Wang, T. Yang, Q. Liu, T. Zhang, S. Zhang, J. Cai, K. Qiao, L. Wang, H. Wang, J. Liu, Intermetallic compounds: Formation mechanism and effects on the mechanical properties of friction stir lap welded dissimilar joints of magnesium and aluminum alloys, Mater. Sci. Eng. A. 802 (2021) 140554. https://doi.org/10.1016/j.msea.2020.140554.

[39] Y. Huang, X. Meng, Y. Xie, L. Wan, Z. Lv, J. Cao, J. Feng, Friction stir welding/processing of polymers and polymer matrix composites, Compos. Part A Appl. Sci. Manuf. 105 (2018) 235–257. https://doi.org/10.1016/j.compositesa.2017.12.005.

[40] G.Y. Li, B.L. Chen, Formation and Growth Kinetics of Interfacial Intermetallics in Pb-Free Solder Joint, IEEE Trans. Components Packag. Technol. 26 (2003) 651–658. https://doi.org/10.1109/TCAPT.2003.817860.

[41] G. Liu, M. Gong, D. Xie, J. Wang, Structures and Mechanical Properties of Al-Al 2 Cu Interfaces, Jom. 71 (2019) 1200–1208. https://doi.org/10.1007/s11837-019-03333-x.

[42] C. Wang, G. Chen, X. Wang, Y. Zhang, W. Yang, G. Wu, Effect of Mg content on the

thermodynamics of interface reaction in C f/Al composite, Metall. Mater. Trans. A Phys. Metall. Mater. Sci. 43 (2012) 2514–2519. https://doi.org/10.1007/s11661-012-1090-z.

[43] C. Li, D. Li, X. Tao, H. Chen, Y. Ouyang, Molecular dynamics simulation of diffusion bonding of Al-Cu interface, Model. Simul. Mater. Sci. Eng. 22 (2014). https://doi.org/10.1088/0965-0393/22/6/065013.

[44] L. Wang, Z. Yang, Y. Cui, B. Wei, S. Xu, J. Sheng, M. Wang, Y. Zhu, W. Fei, Graphene-copper composite with micro-layered grains and ultrahigh strength, Sci. Rep. 7 (2017). https://doi.org/10.1038/srep41896.

[45] Y. He, B. Li, C. Wang, S.X. Mao, Direct observation of dual-step twinning nucleation in hexagonal close-packed crystals, Nat. Commun. 11 (2020) 1–8. https://doi.org/10.1038/s41467-020-16351-0.

[46] E. Mohammad Sharifi, M.H. Enayati, F. Karimzadeh, Fabrication and Characterization of Al - Al 4 C 3 Nanocomposite By Mechanical Alloying, Int. J. Mod. Phys. Conf. Ser. 05 (2012) 480–487. https://doi.org/10.1142/s2010194512002371.

[47] A. Sharma, V.M. Sharma, S. Mewar, S.K. Pal, J. Paul, Friction stir processing of Al6061-SiC-graphite hybrid surface composites, Mater. Manuf. Process. 33 (2018) 795–804. https://doi.org/10.1080/10426914.2017.1401726.

[48] V. Gallegos Orozco, A. Santos Beltrán, M. Santos Beltrán, H. Medrano Prieto, C. Gallegos Orozco, I. Estrada Guel, Effect on microstructure and hardness of reinforcement in al–cu with al4c3 nanocomposites, Metals (Basel). 11 (2021) 1–13. https://doi.org/10.3390/met11081203.

[49] W. Zhou, Z. Zhou, K. Kubota, H. Ono, N. Nomura, A. Kawasaki, Design of high-performance Al4C3/Al matrix composites for electric conductor, Mater. Sci. Eng. A. 798 (2020) 140331. https://doi.org/10.1016/j.msea.2020.140331.

[50] R. Li, H. Kang, Z. Chen, G. Fan, C. Zou, W. Wang, S. Zhang, Y. Lu, J. Jie, Z. Cao, T. Li, T. Wang, A promising structure for fabricating high strength and high electrical conductivity copper alloys, Sci. Rep. 6 (2016) 1–9. https://doi.org/10.1038/srep20799.

[51] S. Kumar, S.K. Pattanayek, S.K. Das, Reactivity-Controlled Aggregation of Graphene Nanoflakes in Aluminum Matrix: Atomistic Molecular Dynamics Simulation, J. Phys. Chem. C. 123 (2019) 18017–18027. https://doi.org/10.1021/acs.jpcc.9b03101.

[52] M.P. Allen, D.J. Tildesley, Computer simulation of liquids, Oxford university press, 2017.

[53] Y. Zhang, N.R. Tao, K. Lu, Effect of stacking-fault energy on deformation twin thickness in Cu-Al alloys, Scr. Mater. 60 (2009) 211–213. https://doi.org/10.1016/j.scriptamat.2008.10.005.

[54] J.T. Lloyd, A dislocation-based model for twin growth within and across grains, Proc. R. Soc. A Math. Phys. Eng. Sci. 474 (2018). https://doi.org/10.1098/rspa.2017.0709.

[55] W.S. Zhao, N.R. Tao, J.Y. Guo, Q.H. Lu, K. Lu, High density nano-scale twins in Cu induced by dynamic plastic deformation, Scr. Mater. 53 (2005) 745–749. https://doi.org/10.1016/j.scriptamat.2005.05.022.

[56] C. Liu, P. Shanthraj, J.D. Robson, M. Diehl, S. Dong, J. Dong, W. Ding, D. Raabe, On the interaction of precipitates and tensile twins in magnesium alloys, Acta Mater. 178 (2019) 146–162. https://doi.org/10.1016/j.actamat.2019.07.046.

[57] J.H. Gosling, O. Makarovsky, F. Wang, N.D. Cottam, M.T. Greenaway, A. Patanè, R.D. Wildman, C.J. Tuck, L. Turyanska, T.M. Fromhold, Universal mobility characteristics of graphene originating from charge scattering by ionised impurities, Commun. Phys. 4 (2021). https://doi.org/10.1038/s42005-021-00518-2.

[58] H. Bishara, S. Lee, T. Brink, M. Ghidelli, G. Dehm, Understanding Grain Boundary Electrical Resistivity in Cu: The Effect of Boundary Structure, ACS Nano. (2021). https://doi.org/10.1021/acsnano.1c06367.

[59] T. Mehner, M. Uland, T. Lampke, Analytical model to calculate the grain size of bulk material based on its electrical resistance, Metals (Basel). 11 (2021) 1–10. https://doi.org/10.3390/met11010021.

[60] G. Greczynski, L. Hultman, X-ray photoelectron spectroscopy: Towards reliable binding energy referencing, Prog. Mater. Sci. 107 (2020) 100591.

https://doi.org/10.1016/j.pmatsci.2019.100591.

[61] V. Borovikov, M.I. Mendelev, A.H. King, R. Lesar, Effect of stacking fault energy on mechanism of plastic deformation in nanotwinned FCC metals, Model. Simul. Mater. Sci. Eng. 23 (2015) 1–19. https://doi.org/10.1088/0965-0393/23/5/055003.

[62] Y.Z. Tian, L.J. Zhao, S. Chen, A. Shibata, Z.F. Zhang, N. Tsuji, Significant contribution of stacking faults to the strain hardening behavior of Cu-15%Al alloy with different grain sizes, Sci. Rep. 5 (2015) 2–10. https://doi.org/10.1038/srep16707.

[63] L. Lu, Y. Shen, X. Chen, L. Qian, K. Lu, Ultrahigh Strength and High Electrical Conductivity in Copper, Science (80-.). 304 (2004) 422–426. https://doi.org/10.1126/science.1092905.

Graphical abstract